Role of heterophase interfaces on local coercivity mechanisms in the magnetic Al0.3CoFeNi complex concentrated alloy

Acta Materialia 246 (2023) 118672

Contents lists available at ScienceDirect

Acta Materialia

journal homepage: www.elsevier.com/locate/actamat

Role of heterophase interfaces on local coercivity mechanisms in the magnetic $Al_{0.3}CoFeNi$ complex concentrated alloy

András Kovács [a,*], Nithin B. Venkataraman [a], Varun Chaudhary [b], Sriswaroop Dasari [c], Thibaud Denneulin [a], R.V. Ramanujan [b], Rajarshi Banerjee [c], Rafal E. Dunin-Borkowski [a]

[a] Ernst Ruska-Centre for Microscopy and Spectroscopy with Electrons and Peter Grünberg Institute, Forschungszentrum Jülich, 52425 Jülich, Germany
[b] School of Materials Science and Engineering, Nanyang Technological University, 639798, Singapore
[c] Department of Materials Science and Engineering, University of North Texas, Denton, TX 76207, USA

ARTICLE INFO

Keywords:
High entropy alloy
Magnetism
Domain wall
Transmission electron microscopy

ABSTRACT

Microstructural features across different length scales have a profound influence on the coercivity of magnetic alloys. Whereas the role of homophase boundaries on the pinning of magnetic domain walls is well established, the influence of heterophase interfaces on domain wall motion is complex and poorly understood. Here, we use state-of-the-art electron microscopy techniques to show that the magnetization reversal process in an $Al_{0.3}CoFeNi$ magnetic complex concentrated alloy (CCA), which is responsible for its coercivity, changes dramatically from a nucleation-type mechanism in the FCC+$L1_2$ state of the CCA, with a domain wall width of 171 nm, to a pinning type mechanism in the microstructure with colonies of FCC/$L1_2$ nanorods embedded in a BCC/B2 matrix, with a domain wall width of 35 nm. Our work reveals that heterophase FCC/BCC interfaces have a much stronger effect on coercivity than isostructural chemically ordered/disordered interfaces and provides a powerful guide to the rational design of microstructure to tune magnetic properties in both complex concentrated alloys and conventional magnetic alloys.

1. Introduction

Complex concentrated alloys (CCAs) or multi-principal-element alloys (MPEAs) or high entropy alloys (HEAs) are a novel class of materials that offer superior functional and structural performance in many applications [1]. Their properties can be tuned over a very wide range as a result of the vast number of possible combinations of elements and processing strategies. Whereas most previous studies of CCAs have focused on their structural properties, much less effort has been paid to understanding their local functional properties.

Soft magnetic materials are key components in industrial applications that include electrical power generation, electrical machines, magnetic shielding and electromagnets [2,3]. High frequency electrical motors require materials with high mechanical strength and superior magnetic properties. However, the low strength of conventional soft magnetic materials limits their use in such applications, particularly in high rotational frequency devices.

Recent research has focused on identifying novel high-strength soft magnets in the HEA domain. Most magnetic CCAs contain Fe, Co and Ni, in combination with other alloying elements. Although some FeCoNi-X (X = Al, Si, Cu, AlSi, AlCu, AlMn, *etc.*) CCAs have promising combinations of magnetic and mechanical properties [4], their magnetic softness generally decreases with increasing mechanical strength, with their coercivity H_c depending sensitively on their composition and microstructure over various length scales. For example, the strength of the $FeCoNi(CuAl)_{0.8}Ga_x$ ($0 < x < 0.08$) HEA improved from 601 MPa for $x = 0$ to 1176 MPa for $x = 0.08$. However, its coercivity increased from 362 to 685.8 A/m [5]. Another important property is saturation magnetization M_s, which increases with diamagnetic Ga content in $FeCoNi(CuAl)_{0.8}Ga_x$ HEAs. Such changes in magnetic and mechanical properties result from the heterogeneous microstructure of these alloys and are not yet understood experimentally.

Here, we study a model $Al_{0.3}CoFeNi$ CCA, whose magnetic and mechanical properties can be tuned by varying the processing conditions [6,7]. The first sample was obtained by solutionizing the alloy at 1250 °C (cold rolling solution annealing or CRSA) to form an FCC+$L1_2$ microstructure. The second sample was obtained by annealing the solutionized alloy at 600 °C for 50 h to form a hierarchical microstructure

* Corresponding author.
E-mail address: a.kovacs@fz-juelich.de (A. Kovács).

https://doi.org/10.1016/j.actamat.2023.118672
Received 5 August 2022; Received in revised form 16 December 2022; Accepted 2 January 2023
Available online 2 January 2023

(CRSA600). The magnetic and mechanical properties of the two alloys are given in Table 1. The large difference in properties (increase in H_c by a factor of >60 and increase in yield strength and hardness by a factor of >2) obtained by changing the heat treatment makes this alloy a model material to understand the influence of *local* variations in composition and microstructure on coercivity using quantitative *in situ* magnetic imaging techniques in the transmission electron microscope (TEM).

2. Experimental

A plate-shaped arc-melted $Al_{0.3}$CoFeNi ingot was procured from ACI Alloys Inc., CA, USA. The composition of the cast ingot was measured to be 9.4Al-30.1Co-31.9Fe-28.6Ni (at.%) using energy dispersive X-ray spectroscopy (EDXS) in a scanning electron microscope. The cast alloy was initially homogenized at 1250 °C for 1 h. Subsequently, all samples were cold rolled to 90%, encapsulated in quartz tubes backfilled with Ar and either solutionized at 1250 °C for 5 min (CRSA) or solutionized and annealed at 600 °C for 50 h (CRSA600), followed by water quenching. Magnetization (M) *vs* magnetic field (H) measurements obtained from the CRSA and CRSA600 samples are shown in Fig. S1 in the Supplementary Materials.

Electron-transparent (<200 nm thick) specimens for TEM investigations were prepared using focused ion beam (FIB) sputtering with Ga in a dual beam scanning electron microscope (FEI Helios 400). A protective C layer was deposited on the surface of the alloys, followed by a conventional lift-off preparation process. The specimens were transferred to Cu Omniprobe grids. Ga-ion-beam-induced surface damage was reduced [8] by subsequently using low energy (<1 keV) Ar ion beam milling (Fischione 1040 Nanomill).

Microstructural and chemical composition analyses were carried out using a probe-aberration-corrected scanning transmission electron microscope (FEI Titan 80-200) equipped with an in-column EDXS system [9] (Super-X technology). High-angle annular dark-field (HAADF) scanning TEM (STEM) and EDXS spectrum images were recorded and processed using ThermoFisher Velox software. The inner semi-angle of the annular dark-field detector was 69.1 mrad for HAADF STEM imaging.

Magnetic imaging of domain structures was carried out in magnetic-field-free conditions (Lorentz mode) by switching off the conventional objective lens of the microscope in an image aberration-corrected TEM (FEI Titan 60-300) [10]. Images were recorded using a 4k direct electron counting detector (Gatan K2 IS) operated in counting mode. Off-axis electron holography was carried out using a single electron biprism. A positive voltage of up to 120 V was applied to the biprism wire, resulting in a 3.2 nm interference fringe spacing and approximately 40% interference fringe contrast. Electron holograms were analyzed using a standard fast Fourier transform algorithm in a custom-made software package written in the Semper image processing language [11].

3. Results

3.1. Microstructure of the CRSA sample

Previous atom probe tomography and TEM studies of the CRSA sample [6] revealed the presence of Al+Ni rich $L1_2$ (ordered FCC) precipitates of average size ~1.95 nm dispersed in an FCC matrix. Fig. 1 (a) shows a composition-sensitive HAADF STEM image (Image intensity $\sim Z^2$, where Z is atomic number) and a corresponding bright-field (BF) STEM image recorded from the same region. The HAADF STEM image confirms the presence of local fluctuations in chemical composition, while the BF STEM image, which is sensitive to diffraction conditions, reveals dense contrast variations that are attributed to the presence of the $L1_2$ precipitates. As this specimen was prepared for magnetic imaging with a large lateral size and a uniform thickness of ~100 nm, many particles contribute to the contrast. The fact that the precipitates are coherent with the matrix is evidenced by the absence of misfit dislocations in the high-resolution HAADF STEM image shown in Fig. 1(b).

3.2. Magnetic imaging of the CRSA sample

The magnetic domain structure was first studied qualitatively using Fresnel imaging at a defocus of 1 mm in magnetic-field-free conditions. Magnetic domain walls are visible in the form of black and white contrast lines in Fig. 1(c). Splitting of vertical domain walls into pairs close to the edge of the specimen is associated with the formation of closure domains to reduce or eliminate energetically-costly stray fields around the specimen. The regular pattern of domain walls results in part from the anisotropic magnetic properties of the sample. As it is difficult to extract quantitative information from the analysis of Fresnel defocus images, off-axis electron holography was used to further study the magnetic properties of the CRSA sample. The technique can be used to recover the phase shift ϕ of the electron wave induced by the projected in-plane component of the magnetic field within and around the specimen [12]. The phase shift can be displayed in the form of a magnetic induction map using contour lines at the positions of equiphase contours and colors. Fig. 1(d) shows a magnetic induction map of closure domains in the lower left corner of Fig. 1(c). (The magnetic and electrostatic contribution to the phase shift were not separated here, as the sample has uniform thickness, resulting in a constant electrostatic contribution to the phase shift). The magnetic induction map shown in Fig. 1(c) confirms the presence of one 180° and two 90° domain walls. The width of the 180° domain wall was determined from the differential $(\partial\phi/\partial x)$ of the recorded phase shift by using a fitting function of the form $y = y_0 \pm a\tanh((x - x_0)/w)$, where y_0, a, x_0 and w are constants obtained from the fit. The domain wall width δ_w is defined as $\delta_w = \pi w$ and is measured to be 171 ± 5 nm in the CRSA sample, which is larger than typical domain wall widths in Co (24 nm), Fe (64 nm) and Ni (82 nm). The electron beam direction is close to perpendicular to the field direction in the magnetic domains, which provides a reliable way to determine the domain wall width in thin TEM specimens.

3.3. Microstructural and magnetic imaging of the CRSA600 sample

Heat treatment of the CRSA600 sample resulted in the formation of a striking nanorod structure comprising FCC+$L1_2$ and BCC+B2 regions, as reported previously [7]. For magnetic imaging, a TEM specimen containing more than one grain was prepared in such a way that magnetic domains oriented both parallel and perpendicular to the nanorods could be studied. Fig. 2(a) shows a low magnification BF TEM image of the CRSA600 sample. Region **I** contains multiple long nanorods of FCC (+

Table 1
Summary of magnetic and mechanical properties of the CRSA and CRSA600 samples of the $Al_{0.3}$CoFeNi complex concentrated alloy.

	Structure	M_s emu/g	H_c Oe	D_c μm	δ_w nm	Hardness VHN	Yield stress MPa	Tensile strength MPa	Plastic strain %
CRSA	FCC/$L1_2$	131.4	2.5	8	171	196.6	457	853	76
CRSA600	FCC/$L1_2$+BCC/B2	138.7	160	0.1	35	513	1074	1302	8

M_s is the saturation magnetization, H_c is the coercivity, D_c is the magnetic domain size measured using TEM, δ_w is the magnetic domain wall width, VHN is the Vickers hardness number.

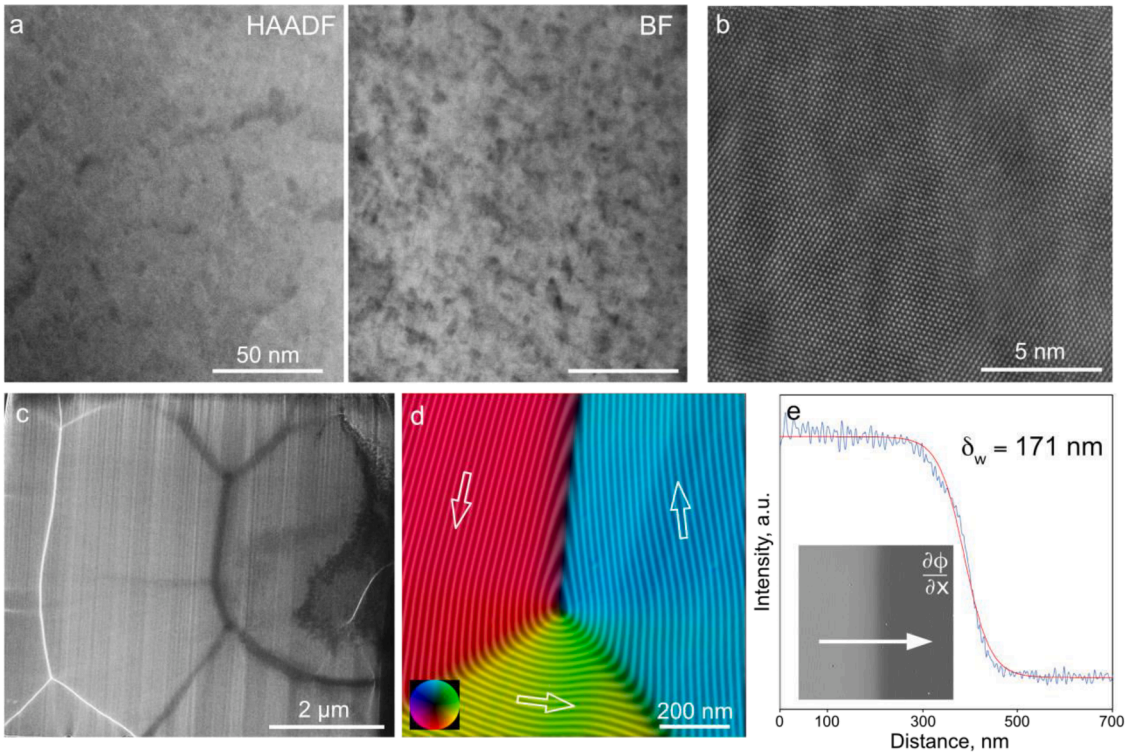

Fig. 1. Microstructural and magnetic imaging of the CRSA sample (a) HAADF STEM and BF STEM images show local variations in chemical composition and diffraction contrast originating from Ni/Al-rich precipitates. The HAADF detector inner semi-angle was 69 mrad for the HAADF STEM image. (b) Atomic-resolution HAADF STEM image. (c) Fresnel defocus image showing black and white contrast at the positions of magnetic domain walls recorded in magnetic-field-free conditions at a defocus of 1 mm. (d) Magnetic induction map of a flux closure region measured using off-axis electron holography. The contour spacing is π radians. Arrows and colors indicate projected in-plane magnetic field directions. (e) Magnetic domain wall width measurement using the (inset) phase shift differential across the 180° wall shown in (d). The magnetic domain wall width (δ_w) is determined to be 171 ± 5 nm. (For interpretation of the references to color in this figure legend, the reader is referred to the web version of this article.)

$L1_2$) colonies in a BCC (+ B2) matrix, whose width varies between 50 and 200 nm. Region **II** appears to contain equidimensional grains, which correspond to the nanorods viewed along their long axes.

Fig. 2(b, c) shows selected area electron diffraction (SAED) patterns recorded from regions **I** and **II** using an aperture of size ~1 μm. Based on the SAED patterns, region **I** is oriented along [110]FCC/[111]BCC, while region **II** is oriented along [001]FCC/[001]BCC. The diffraction spots from the FCC and BCC phases overlap each other, indicating a close epitaxial relationship. By bringing each phase separately to a zone axis orientation (see Fig. S3), a mistilt of ~3° was measured between the FCC and BCC columns. Red triangles in Fig. 2(b, c) mark weak superlattice reflections, which are associated with $L1_2$ and B2 ordering in the FCC and BCC phases, respectively.

Fig. 2(d, e) shows Fresnel defocus images of representative magnetic domain structures in the two regions recorded in magnetic-field-free conditions. Strikingly, the magnetic domain walls in region **I** are regular and follow the straight heterophase interfaces closely. Inside the columns, fine black and white streaks are visible. In contrast, region **II** contains a highly dense random network of magnetic domain walls. The Fresnel defocus images cannot alone be used to determine unambiguously whether the streaks in region **I** are magnetic or structural in origin. Fig. S4 in the Supplementary Materials shows a large-field-of-view image of the projected in-plane magnetic induction in region **I** determined from a pair of Fresnel defocus images using the transport-of-intensity equation.

3.4. Correlation between magnetic domains and microstructure

STEM EDXS spectrum imaging was used to correlate the variations in composition associated with the FCC and BCC phases with the positions of magnetic domains in the CRSA600 sample. Fig. 3(a) shows a BF STEM image and corresponding Co, Fe, Ni and Al maps recorded from region **II**, showing that the Co–Fe-rich BCC phase is the matrix, in which Ni–Al-rich FCC columns are distributed. The nanorod structure shown in Fig. 3 (b) corresponds to this microstructure viewed from the side (in region **I**).

The EDXS maps reveal compositional fluctuations in the Ni–Al-rich FCC columns, as well as additional Ni and Al enrichment parallel to the FCC/BCC interphase boundaries. Fig. 3(c) shows higher magnification EDXS maps of the fluctuations in chemical composition, which consist of Co–Fe-rich and Ni–Al-rich regions in the FCC columns. An additional Ni–Al-rich region is present close to the interface and parallel to the interphase boundary. The Fe and Co distribution in the BCC column is also not uniform, as shown in the maps in Fig. 3(a) and in Fig. S3 in the Supplementary Materials. The apparently homogenous distribution of Fe and Co in the BCC phase in Fig. 3(c) results from the small field of view and possible overlap between different regions in the electron beam direction. Fig. 3(d) shows EDXS line scans across the interface between the BCC and FCC columns, with the heterophase boundary marked by a vertical dashed line. Within the FCC column, an approximately 7-nm-wide Ni–Al-rich and Co–Fe-poor region runs parallel to the FCC/BCC interface. Based on the results shown in Fig. 3 and on atom probe tomography (APT) reconstructions shown in Fig. S2 in the Supplementary Materials, the morphology of the FCC and BCC based regions can be described as colonies of FCC/$L1_2$ nanorods embedded in a BCC/B2 matrix. Within the FCC/$L1_2$ nanorods, as well as within the BCC/B2 matrix, there is a finer-scale decomposition into ordered and disordered regions. The morphology of these ordered $L1_2$ and B2 regions appears to be lamellar based on the APT reconstructions. Fig. 3(e) shows a high-resolution HAADF STEM image recorded from the same region as the maps in Fig. 3(c). The image shows a uniform lattice in both grains. The

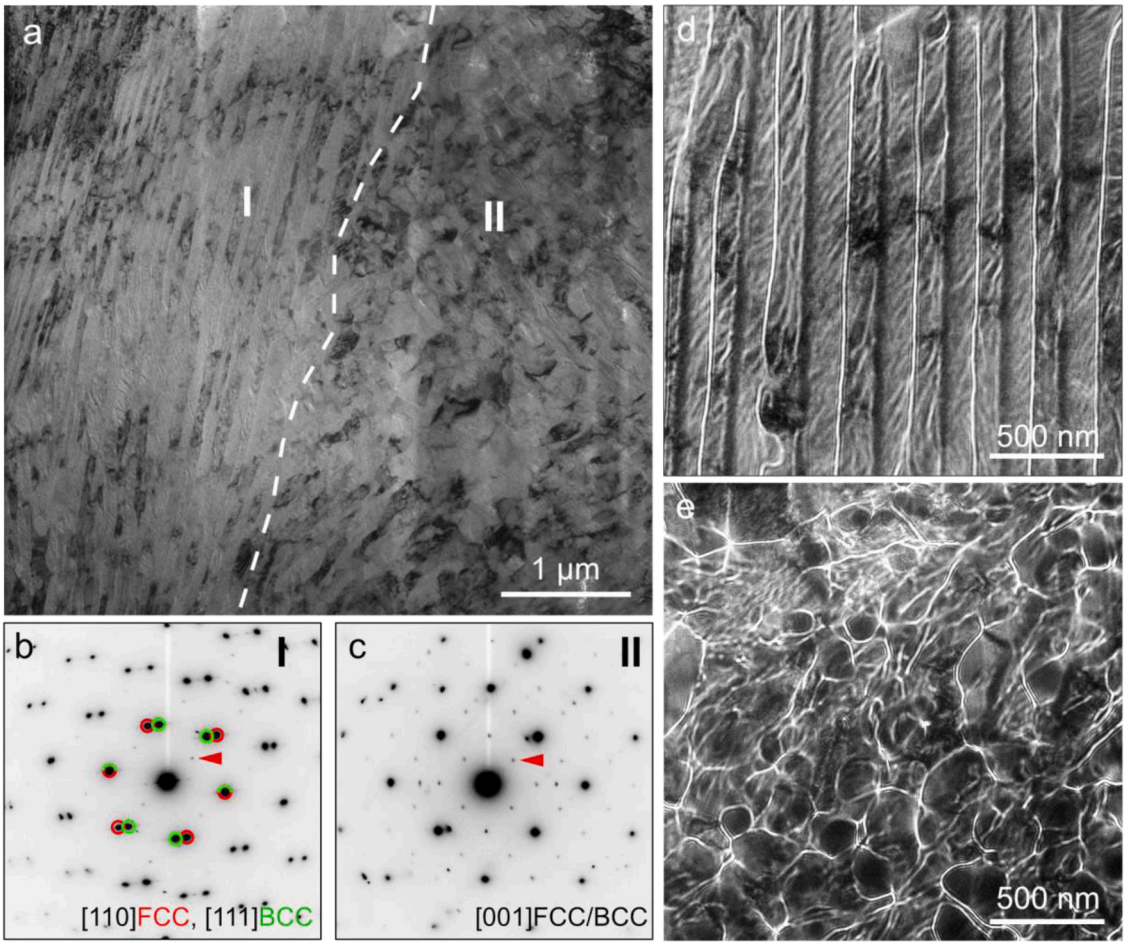

Fig. 2. Microstructural and magnetic imaging of the CRSA600 sample (a) BF TEM image showing the nanorods viewed from the side (**I**) and parallel to their long directions (**II**). (b, c) SAED patterns recorded from regions **I** and **II**. Red arrows mark superlattice reflections associated with $L1_2$ and B2 ordering. (d, e) Fresnel images recorded at a defocus of 0.25 mm from regions **I** and **II**, respectively. (For interpretation of the references to color in this figure legend, the reader is referred to the web version of this article.)

orientation of the phases (visible in the digital diffractogram shown as an inset to Fig. 3(e)) is similar to that in the SAED pattern from region **I** in Fig. 2(b).

The magnetic domains in the CRSA600 sample were further analyzed using off-axis electron holography. Fig. 4(a) shows an amplitude image of the columns, which were tilted slightly away from the crystallographic zone axis to reduce diffraction contrast. In order to study the magnetic domains, the electrostatic and magnetic contributions to the phase shift were separated by using a cartridge-based specimen holder [13] to record pairs of electron holograms before and after turning the TEM specimen over. Half of the sum and half of the difference between each pair of phase images were then used to separate the electrostatic and magnetic contributions to the phase shift, respectively. Fig. 4(b) shows a magnetic induction map created from a magnetic phase image of the magnetic domain walls, which overlap with the heterophase FCC/BCC boundaries in the specimen (Fig. 2(d)). Identical location chemical mapping using EDXS was used to confirm the compositions of the phases (see Fig. S3 in the Supplementary Materials). The downward-oriented magnetic domains, which are present in the FCC+$L1_2$ columns, contain straight magnetic contour lines. Closer inspection of the contour lines and colors in the magnetic induction map in Fig. 4(b) reveals small variations in magnetic properties in the FCC columns, which may be associated with the presence of ordered $L1_2$ regions. In contrast, the observation of well-defined regions that have no magnetic field lines in the BCC+B2 columns indicates the presence of weakly magnetic or non-magnetic inclusions. EDXS spectrum imaging (Fig. S3) confirms that these regions correspond to the locations of the Ni–Al-rich inclusions.

The width of the magnetic domain walls pinned at the grain boundaries in the CRSA600 sample was determined, using the phase differential method described above, to be $\delta_w = 35 \pm 3$ nm, as shown in Fig. 4(c). This value is almost 5 times smaller than that measured in the CRSA sample. In a simple single-phase ferromagnetic system, the domain wall width is described by the expression $\delta_w \sim \sqrt{A/K_{eff}}$, where A is the exchange stiffness and K_{eff} is the effective magnetic anisotropy. However, the CRSA600 sample contains several phases with different magnetic properties. In addition, the magnetic domain walls overlap with the Al–Ni-rich enrichment between the FCC and BCC columns revealed by EDXS (Fig. 3(c)).

4. Discussion

Magnetism in HEAs can be a complex phenomenon, especially in the presence of hierarchical multi-phase microstructures over multiple length scales, which in turn result from competing phase stabilities between solid solution and ordered phases. The possibility to combine transition metals with other elements in the periodic table and different processing parameters provides a wide range of opportunities to tailor the magnetic and functional properties of HEAs [14].

In the present non-equimolar $Al_{0.3}CoFeNi$ CCA, solid state decomposition induced by thermomechanical treatment results in the formation of a eutectoid-like microstructure consisting of FCC+$L1_2$ nanorods

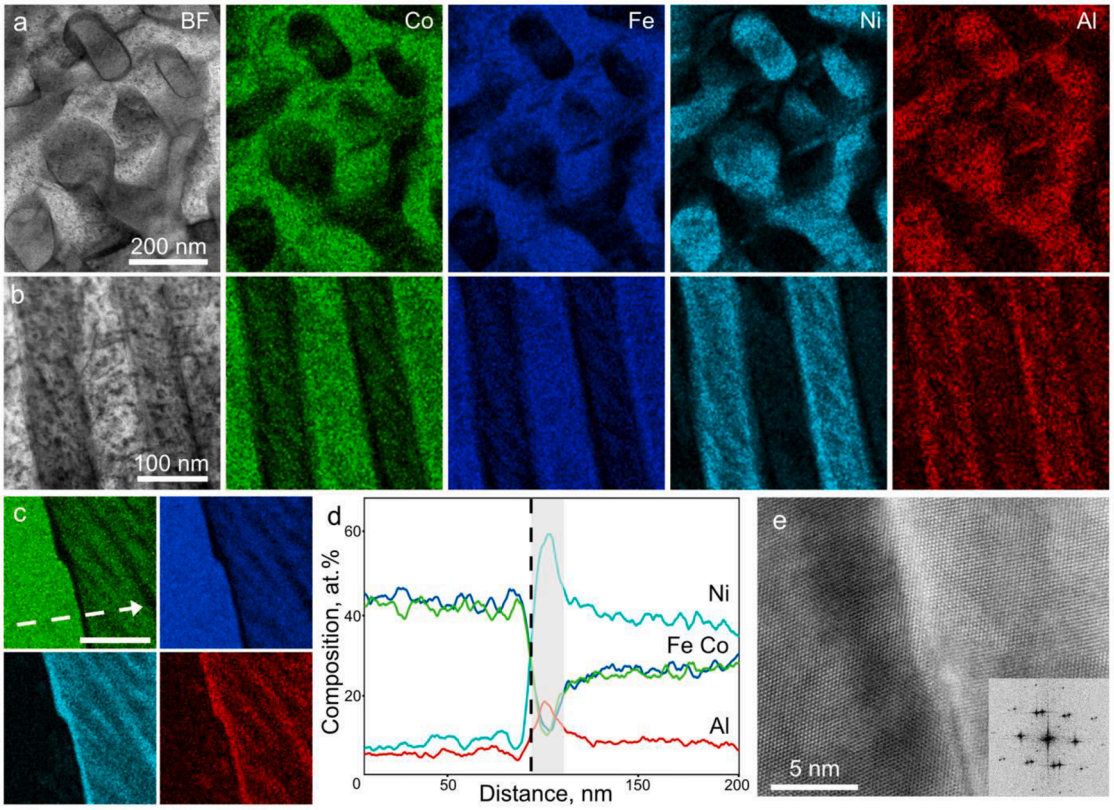

Fig. 3. Microstructure and chemical composition of the nanorod structure in the CRSA600 sample (a, b) BF STEM images and corresponding Co, Fe, Ni and Al EDXS maps recorded from (a) region **II** and (b) region **I**. (c) Higher magnification EDXS maps of the interface between the BCC and FCC columns. The scale bar is 100 nm. (d) Elemental distribution across the interface (marked by a dashed line) extracted from the EDXS spectrum images shown in (c). The EDXS composition measurement error is <10%. The shaded area is rich in Ni and Al and depleted in Fe and Co. (e) High-resolution HAADF STEM image of the interface. The inset shows a digital diffractogram of the crystallographic relationship between the FCC and BCC phases.

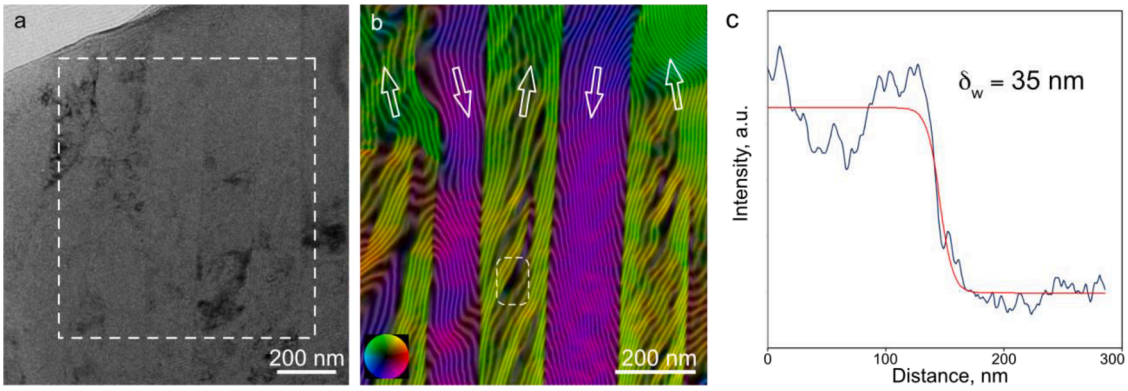

Fig. 4. Magnetic domains in the CRSA600 sample. (a) Amplitude image of the FCC and BCC columns. (b) Magnetic induction map recorded using off-axis electron holography from the marked region in (a), showing alternating magnetic field directions in the domains. Colors and arrows indicate the projected in-plane magnetic field directions. Note the regions with lower densities of magnetic field lines in the BCC columns. The upside-down 'Y'-shaped region (marked by dashed white lines) is confirmed to be Ni–Al-rich from EDXS measurements (Fig. S3 in the Supplementary Materials). (c) Line scan obtained from the phase differential (not shown) used to measure the magnetic domain wall width δ_w as 35 ± 3 nm. (For interpretation of the references to color in this figure legend, the reader is referred to the web version of this article.)

in a BCC+B2 matrix. Table 1 summarizes the magnetic and mechanical properties of the CRSA and CRSA600 samples. Thermomechanical treatment of the CRSA600 sample increases the coercivity (H_c) by a factor of 64. High spatial resolution magnetic characterization reveals that the average magnetic domain size (D_c) in the thin TEM specimens is reduced by an order of magnitude in the CRSA600 sample as result of the presence of magnetic domain walls at heterophase boundaries separating the FCC and BCC phases. Furthermore, the magnetic domain wall width is reduced significantly from 171 ± 5 to 35 ± 3 nm.

The different length scale of chemical ordering and phase separation in the CRSA and CRSA600 samples has a significant effect on the observed magnetic states (Figs. 1 and 2). The CRSA sample (Fig. 1) exhibits rapid variations in composition (on a scale of <20 nm) and a domain wall width of 171 nm, suggesting that homophase interfaces in the FCC alloy are ineffective at pinning magnetic domain walls, leading to low coercivity. In contrast, in the CRSA600 sample the presence of

FCC and BCC phases with different compositions results in different local magnetic properties. In the FCC nanorods, the Ni–Al-rich ordered $L1_2$ phase displays magnetic field lines that are straight and contain only slight angular variations, as shown in Fig. 4(b). In contrast, the Ni–Al-rich ordered B2 regions in the BCC phase have a strong effect on the magnetic induction (Fig. 4(b)), as the density of the magnetic field lines is reduced at the locations of these ordered phases. The saturation magnetization of the two samples is similar, with a slight increase in CRSA600 (Table 1) that can be attributed to the presence of the BCC phase. The pinning of magnetic domain walls at heterophase FCC/BCC boundaries in the CRSA600 sample is influenced by crystallographic and compositional transitions across these boundaries, as well as by the enrichment of Ni and Al in the FCC phase along the boundaries. The presence of the boundaries results in a relatively narrow domain wall width of 35 nm in the CRSA600 sample.

Our microstructural and magnetic observations suggest that the magnetization reversal mechanism that is responsible for the coercivity changes from nucleation-type in the CRSA sample to pinning-type in the CRSA600 sample. In order to validate this hypothesis, *in situ* magnetization reversal experiments were carried out inside the TEM. An in-plane component of the applied magnetic field was obtained by exciting the vertical magnetic field of the objective lens of the microscope to a pre-calibrated value [15]. The sample was then tilted between -30° and $+30^\circ$ to apply an effective in-plane magnetic field and to observe magnetization reversal.

Fig. 5 shows a selection of Fresnel defocus images of the magnetization reversal process in the CRSA and CRSA600 samples displayed as a function of effective in-plane magnetic field. In the CRSA sample (Fig. 5 (a-e)), magnetic domain walls (marked by arrows in Fig. 5(a, b)) nucleate at the edge of the specimen and move across the field of view without interruption. The full cycle of the reversal experiment can be found in the Supplementary Materials. Successive experiments showed similar movement and a lack of domain wall pinning. In the CRSA600 sample, at the maximum in-plane field of approximately 600 mT TEM imaging was still possible, but the field was insufficient to generate a saturated state without any magnetic domain walls. Fig. 5(f) shows the initial magnetic domain structure in the CRSA600 sample at −81 mT. There is no substantial change as the effective in-plane field is decreased to 0 mT (Fig. 5(g)). An increase in field to +81 mT results in a few switching events at domain walls (yellow arrowheads in Fig. 5(g, h)). At these locations, the domain wall contrast changes to the opposite sign, suggesting that the magnetization direction switched in these domains. This process extends to adjacent domains as the field is increased to +133 mT. The arrowheads in Fig. 5(i, j) mark domain walls that switch at this stage. It is interesting to note that magnetization switching forms domain walls that contain both black and white contrast, which are so-called Bloch caps in 180° domain walls (dashed ovals in Fig. 5(h, j)).

The *in situ* magnetizing experiments presented in Fig. 5 confirm that the magnetization reversal process changes from nucleation-type in the CRSA sample to pinning-type in the CRSA600 sample as a result of phase decomposition after prolonged annealing at 600 °C for 50 h, leading to the formation of a nanorod microstructure with heterophase FCC/BCC interfaces.

The present study provides fundamental insight into the role of interphase interfaces on magnetization reversal mechanisms through domain wall pinning. Fig. 6 summarizes schematically the basic structural features in the samples that lead to fundamentally different magnetic properties. Heterophase interfaces between phases with different crystal structures (*e.g.*, FCC/BCC) are effective at pinning magnetic domain walls and consequently increase coercivity. This pinning mechanism is particularly effective when the heterophase interfaces occur at near-periodic intervals in the microstructure on deep-sub-μm length scales, such as in the present nanorod microstructure. In contrast, homophase interfaces of order/disorder type, such as FCC+$L1_2$ or BCC+B2, do not hinder magnetic domain wall motion significantly. This insight can be used to provide guidance for the design of both high entropy and conventional alloys with desired combinations of magnetic and mechanical properties. For example, if high mechanical strength is desired while preserving low coercivity then the introduction of a large volume fraction of ordered precipitates within a parent solid solution can be effective, especially if misfit strain can be minimized. Similarly, higher coercivity can be produced by the presence of a nanorod structure with heterophase boundaries, while uniaxial magnetic anisotropy can be tailored through the introduction of strain or magnetic-field-induced anisotropy during the annealing process. Such strategies for tuning the coercivity of high entropy alloys are analogous to those used for Alnico-type hard magnets [16] and for hard magnets based on Sm-Co.

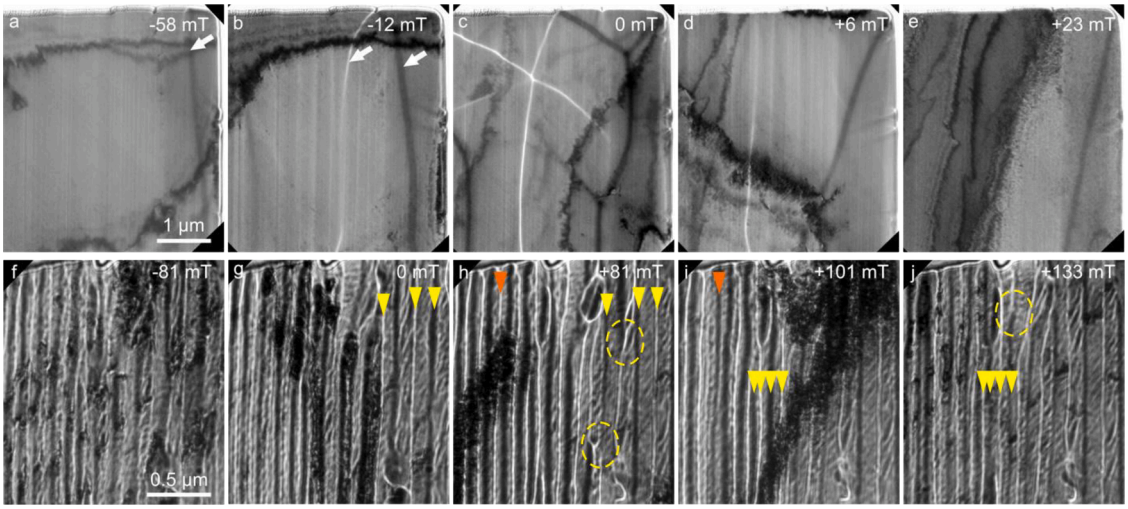

Fig. 5. Magnetization switching processes. Fresnel defocus images showing (a-e) nucleation-type magnetization reversal in the CRSA sample and (f-j) pinning-type magnetization reversal in the CRSA600 sample. The effective in-plane field was applied in the horizontal direction and is indicated in the images. The defocus value is 500 μm. In (a) and (b), arrows mark the positions of magnetic domain walls. In (g-j), yellow and orange arrowheads mark the positions of magnetic domain walls that switch. Dashed ovals mark the positions of Bloch caps in domain walls. Note the presence of diffraction contrast (in particular, wide bands of dark contrast associated with bending of the sample) in addition to magnetic domain wall contrast. (For interpretation of the references to color in this figure legend, the reader is referred to the web version of this article.)

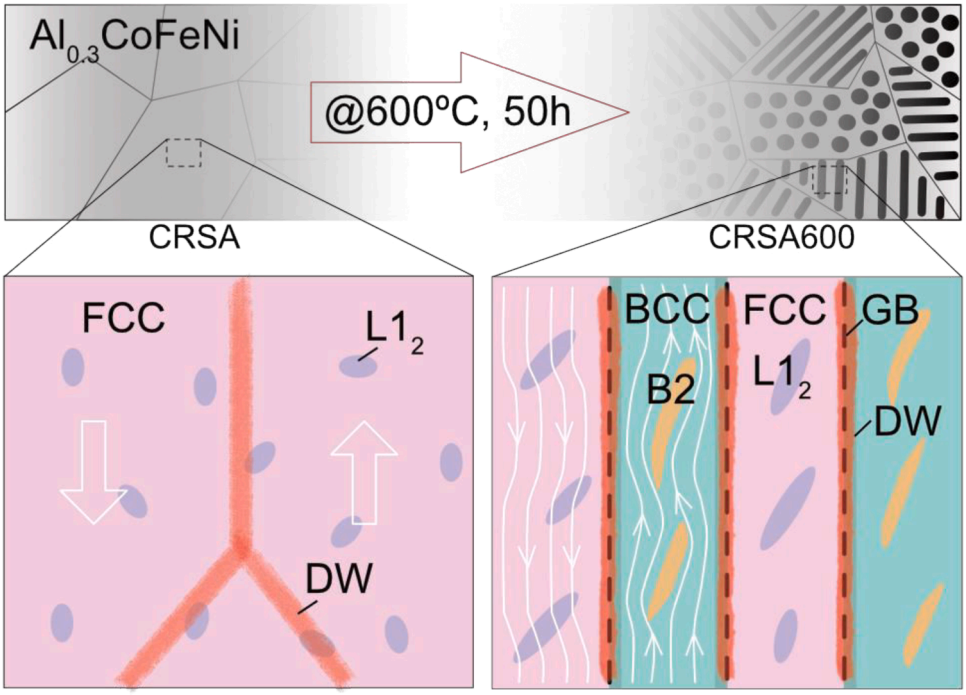

Fig. 6. Schematic diagram showing the structural and magnetic characteristics of the $Al_{0.3}$CoFeNi complex concentrated alloy samples. Magnetic domain walls (DWs) form and move freely within the FCC+$L1_2$ alloy, while they are pinned at heterophase boundaries between the FCC+$L1_2$ and BCC+B2 regions. In the BCC+B2 region, magnetic field lines (white, arrowed) embrace weakly magnetic B2 precipitates.

5. Conclusions

Our high spatial resolution investigation of the microstructural and magnetic behavior of an $Al_{0.3}$CoFeNi complex concentrated alloy has revealed an intricate coupling between the presence of a hierarchical multi-length-scale multi-phase microstructure and the motion of magnetic domain walls. High-resolution *in situ* techniques show that the magnetization reversal process, which is responsible for coercivity, changes from a nucleation-type mechanism in the FCC+$L1_2$ microstructure of this alloy, with a domain wall width of 171 nm, to a pinning-type mechanism in the nanorod microstructure of the same alloy, with a domain wall width of 35 nm. Significantly, heterophase FCC/BCC nanoscale interfaces strongly pin magnetic domain walls, increasing coercivity when compared to homophase chemically ordered/disordered interfaces. These results provide a powerful guide for the rational design of microstructure to tune the magnetic and mechanical properties of both high entropy alloys and more conventional magnetic alloys.

Declaration of Competing Interest

The authors declare that they have no known competing financial interests or personal relationships that could have appeared to influence the work reported in this paper.

Acknowledgments

This project has received funding from the European Research Council under the European Union's Horizon 2020 research and innovation program (Grant No. 856538, project "3D MAGiC'') and the Deutsche Forschungsgemeinschaft (DFG, project-IDs 405553726). The support of the AME Programmatic Fund by the Agency for Science, Technology and Research, Singapore under Grant No. A1898b004 is acknowledged. The UNT team has been supported by the US Air Force Office of Scientific Research (AFOSR) under grants FA9550-17-1-0395 and FA9550-21-1-0304. The authors acknowledge the Materials Research Facility (MRF) at the University of North Texas.

Supplementary materials

Supplementary material associated with this article can be found, in the online version, at doi:10.1016/j.actamat.2023.118672.

References

[1] E.P. George, D. Raabe, R.O. Ritchie, High-entropy alloys, Nat. Rev. Mater. 4 (2019) 515.
[2] M.E. McHenry, M.A. Willard, D.E. Laughlin, Amorphous and nanocrystalline materials for applications as soft magnets, Prog. Mater. Sci. 44 (1999) 291.
[3] V. Chaudhary, S.A. Mantri, R.V. Ramanujan, R. Banerjee, Additive manufacturing of magnetic materials, Prog. Mater. Sci. 114 (2020), 100688.
[4] V. Chaudhary, R. Chaudhary, R. Banerjee, R.V. Ramanujan, Accelerated and conventional development of magnetic high entropy alloys, Mater. Today 49 (2021) 231.
[5] Z. Li, H. Xu, Y. Gu, M. Pan, L. Yu, X. Tan, X. Hou, Correlation between the magnetic properties and phase constitution of FeCoNi(CuAl)0.8Gax ($0 \leq x \leq 0.08$) high-entropy alloys, J. Alloys Compd. 746 (2018) 285.
[6] S. Dasari, A. Jagetia, A. Sharma, M.S.K.K.Y. Nartu, V. Soni, B. Gwalani, S. Gorsse, R. Banerjee, Tuning the degree of chemical ordering in the solid solution of a complex concentrated alloy and its impact on mechanical properties, Acta Mater. 212 (2021), 116938.
[7] S. Dasari, B. Gwalani, A. Jagetia, V. Soni, S. Gorsse, R. Banerjee, Hierarchical eutectoid nano-lamellar decomposition in an $Al_{0.3}$CoFeNi complex concentrated alloy, Sci. Rep. 10 (2020) 4836, https://doi.org/10.1038/s41598-020-61538-6.
[8] P.E. Fischione, R.E.A. Williams, H.L. Genc, A. Fraser, R.E. Dunin-Borkowski, M. Luysberg, C.S. Bonifacio, A. Kovács, A small spot, inert gas, ion milling process as a complementary technique to focused ion beam specimen preparation, Microsc. Microanal. 23 (2017) 782.
[9] Ernst Ruska-Centre for Microscopy and Spectroscopy with Electrons, FEI Titan G2 80-200 CREWLEY, J. Large-Scale Res. Facil. 2 (2016) A43.
[10] Ernst Ruska-Centre for microscopy and spectroscopy with electrons, J. Large-Scale Res. Facil. 2 (2016) A44.
[11] W.O. Saxton, T.J. Pitt, M. Horner, Digital image processing: the Semper system, Ultramicroscopy 3 (1979) 343.
[12] A. Kovács (Ed.), Dunin-Borkowski, in Handbook of Magnetic Materials, Chapter 2: Magnetic Imaging of Nanostructures Using Off-Axis Electron Holography, Elsevier, 2018, pp. 59–153, https://doi.org/10.1016/bs.hmm.2018.09.001.
[13] P. Diehle, A. Kovács, T. Duden, R. Speen, K.Ž. Soderžnik, R.E. Dunin-Borkowski, A cartridge-based turning specimen holder with wireless tilt angle measurement for magnetic induction mapping in the transmission electron microscope, Ultramicroscopy 220 (2021), 113098.
[14] Q. Lan, A. Kovács, J. Caron, H. Du, D. Song, S. Dasari, B. Gwalani, V. Chaudhary, R. V. Ramanujan, R. Banerjee, R.E. Dunin-Borkowski, Highly complex magnetic

behavior resulting from hierarchical phase separation in AlCo(Cr)FeNi high-entropy alloys, IScience 25 (2022), 104047.

[15] L.A. Rodríguez, C. Magén, E. Snoeck, C. Gatel, L. Marín, L. Serrano-Ramón, J. L. Prieto, M. Muñoz, P.A. Algarabel, L. Morellon, J.M.D. Teresa, M.R. Ibarra, Quantitative *in situ* magnetization reversal studies in Lorentz microscopy and electron holography, Ultramicroscopy 134 (2013) 144.

[16] L. Zhou, M.K. Miller, P. Lu, L. Ke, R. Skomski, H. Dillon, Q. Xing, A. Palasyuk, M. R. McCartney, D.J. Smith, S. Constantinides, R.W. McCallum, I.E. Anderson, V. Antropov, M.J. Kramer, On spinodal decomposition in alnico - A transmission electron microscopy and atom probe tomography study, Acta Mater. 74 (2014) 224.